New Journal of Physics
The open access journal at the forefront of physics

Deutsche Physikalische Gesellschaft DPG
IOP Institute of Physics

Published in partnership with: Deutsche Physikalische Gesellschaft and the Institute of Physics

OPEN ACCESS

RECEIVED
14 November 2019

REVISED
21 January 2020

ACCEPTED FOR PUBLICATION
10 February 2020

PUBLISHED
19 March 2020

Original content from this work may be used under the terms of the Creative Commons Attribution 4.0 licence.

Any further distribution of this work must maintain attribution to the author(s) and the title of the work, journal citation and DOI.

PAPER

Waveform control of currents in graphene by chirped few-cycle lasers

Erheng Wu[1,2,4], **Chaojin Zhang**[3], **Zhanshan Wang**[1] and **Chengpu Liu**[2,4,5]

[1] China MOE Key Laboratory of Advanced Micro-structured Materials, Institute of Precision Optical Engineering, School of Physics Science and Engineering, Tongji University, Shanghai 200092, People's Republic of China
[2] State Key Laboratory of High Field Laser Physics, Shanghai Institute of Optics and Fine Mechanics, Chinese Academy of Sciences, Shanghai 201800, People's Republic of China
[3] School of Physics and Electronic Engineering, Jiangsu Normal University, Xuzhou 221116, People's Republic of China
[4] University of Chinese Academy of Sciences, Beijing 100049, People's Republic of China
[5] Author to whom any correspondence should be addressed.

E-mail: chpliu@siom.ac.cn

Keywords: Coherent control, strong electromagnetic field effects, ultrafast phenomena

Abstract

The residual current density in monolayer graphene driven by an intense few-cycle chirped laser pulse is investigated via numerical solution of the time-dependent Schrödinger equation in the light-field-driven regime. Strikingly, it is found that a purely chirped laser pulse breaks the inversion symmetry in graphene, generating a residual directional current, which is absent for a Fourier-transform limited pulse (2017 *Nature* **550** 224) and is attributed to the chirp-dependent Landau–Zener–Stückelberg interference among different quantum pathways in the reciprocal space. Moreover, the directionality of such a current changes with laser chirp rate following a sine-functional way, which possibly provides a novel application in ultrafast photo-electronics based on two-dimensional materials.

1. Introduction

Quite recently with the occurrence of atomically-thin materials, the interaction of a strong electric field with transparent materials early introduced by Zener [1] and later developed by Keldysh [2] and others, has drawn a renewed attention [3], especially in the light-field-driven regime [4–7], where electron interband transitions are fundamentally influenced by electron intraband dynamics, and the instantaneous light field (waveform), instead of the cycle-averaged light intensity, dominates the electron dynamics [8–17].

For example, in zero-bandgap atomically-thin graphene [7], a non-monotonic increase of carrier-envelop-phase (CEP)-dependent current with field strength, quite different from the monotonic one under a weak field [18], is disclosed. Since the CEP influences the light-field waveform and thus the electron dynamics, delayed pulse-superposition [19] and pulse shaping techniques [20, 21] could take the similar role of CEP.

Therefore, here an chirped few-cycle pulse [22] instead of the transform-limited one [7] is again to investigate the current in monolayer graphene to check whether such a non-monotonic increase pattern still keeps or not. The detailed simulation and theoretical analysis disclose that a purely chirped laser pulse breaks the inversion symmetry in graphene, generating a residual directional current. The behind mechanism is the chirp-dependent Landau–Zener–Stückelberg (LZS) [23] interference among different quantum pathways in the reciprocal space on the sub-cycle timescale. Moreover, such a residual current is sensitive to the exact light field waveform and its directionality can be controlled by the chirp rate, following a sine-functional way, which possibly finds novel application in ultrafast photo-electronics based on two-dimensional materials.

2. Theory and model

2.1. Band structure of graphene

The whole light-field-driven electron dynamics in monolayer graphene is investigated using a nearest-neighbor tight-binding model [7, 21]. The lattice structure of graphene in the position space and the reciprocal vector

© 2020 The Author(s). Published by IOP Publishing Ltd on behalf of the Institute of Physics and Deutsche Physikalische Gesellschaft

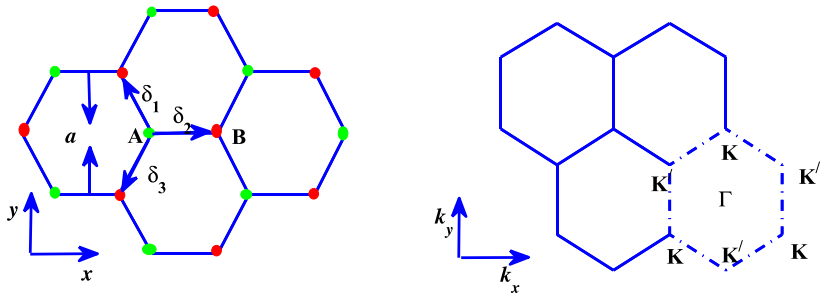

Figure 1. Lattice structure of monolayer graphene in (a) position space or (b) reciprocal vector space. A unit cell contains two carbon atoms at subsides A and B, and the positions of three nearest atoms neighboring around A are $\delta_1 = (-\frac{a}{2\sqrt{3}}, \frac{a}{2})$, $\delta_2 = (\frac{a}{\sqrt{3}}, 0)$ and $\delta_3 = (-\frac{a}{2\sqrt{3}}, -\frac{a}{2})$. The first Brillouin zone (BZ) around Γ is indicated by dashed lines.

space are described in figures 1(a) and (b), respectively. The positions of the nearest three atoms neighboring around a carbon atom at subsite A are $\delta_1 = (-\frac{a}{2\sqrt{3}}, \frac{a}{2})$, $\delta_2 = (\frac{a}{\sqrt{3}}, 0)$ and $\delta_3 = (-\frac{a}{2\sqrt{3}}, -\frac{a}{2})$ with a lattice constant $a = 0.246$ nm. In order to obtain the electronic band structure, the p_z atomic orbital is generally adopted to form a Bloch wave function. Thus, the corresponding field-free electron Hamiltonian is written as

$$H_0 = \begin{bmatrix} 0 & -\varepsilon_h f(\mathbf{k}) \\ -\varepsilon_h f^*(\mathbf{k}) & 0 \end{bmatrix}, \tag{1}$$

in which $\varepsilon_h = 3.0$ eV is the hopping integral, $\mathbf{k} = [k_x, k_y]$ is the initial wave vector, and $f(\mathbf{k}) = \exp(\mathrm{i}ak_x/\sqrt{3}) + 2\exp(-\mathrm{i}ak_x/2\sqrt{3})\cos(k_y a/2)$ determining the symmetric property of a lattice structure. The eigen-energies of conduction and valence bands, $E_c(\mathbf{k}) = \varepsilon_h|f(\mathbf{k})|$ and $E_v(\mathbf{k}) = -\varepsilon_h|f(\mathbf{k})|$, can be directly obtained by diagonalizing $\mathbf{H}_0$ with the corresponding basis functions of

$$\Psi^v_{\mathbf{k}} = \frac{1}{\sqrt{2}}\begin{bmatrix} \exp(\mathrm{i}\theta_{\mathbf{k}}/2) \\ \exp(-\mathrm{i}\theta_{\mathbf{k}}/2) \end{bmatrix}, \Psi^c_{\mathbf{k}} = \frac{1}{\sqrt{2}}\begin{bmatrix} -\exp(\mathrm{i}\theta_{\mathbf{k}}/2) \\ \exp(-\mathrm{i}\theta_{\mathbf{k}}/2) \end{bmatrix}. \tag{2}$$

Here, $\theta_{\mathbf{k}}$ is phase factor and defined as $\theta_{\mathbf{k}} = \frac{f(\mathbf{k})}{|f(\mathbf{k})|}$.

2.2. Electron dynamics under external field

The electron dynamics under an ultrashort external field, linearly polarized along the x direction, is coherent, and can be well described by the time-dependent Schrödinger equation (TDSE)

$$i\hbar\frac{\mathrm{d}}{\mathrm{d}t}\Psi = H\Psi \tag{3}$$

with $H = H_0 - e\mathbf{E}(t)\mathbf{r}$. It is convenient to solve the TDSE on the basis of Houston states $\Phi_{\mathbf{k}}$ [24]. The solution can be first expanded as $\Psi_{\mathbf{k}} = \sum_{\beta=c,v} a_{\beta,\mathbf{k}}(t)\exp(\int_{-\infty}^{\infty} E_\beta(\mathbf{k}(t'))\mathrm{d}t')\Phi_\beta(\mathbf{k}(t))$, with $\mathbf{k}(t) = \mathbf{k} - \frac{e}{\hbar}\int_{-\infty}^{t} E_x(t')\mathrm{d}t'$, following the Bloch acceleration theory. Then, after substituting $\Psi_{\mathbf{k}}$ into equation (3), the temporal evolution of probability amplitude $a_{\beta,k}(t)$ is obtained as

$$\begin{aligned} \dot{a}^c_{\mathbf{k}}(t) &= -\mathrm{i}\Omega_R(\mathbf{k}(t))\exp(-\frac{\mathrm{i}}{\hbar}\int_{-\infty}^{t}\nabla E(\mathbf{k}(t'))\mathrm{d}t')a^v_{\mathbf{k}}(t), \\ \dot{a}^v_{\mathbf{k}}(t) &= -\mathrm{i}\Omega_R(\mathbf{k}(t))\exp(\frac{\mathrm{i}}{\hbar}\int_{-\infty}^{t}\nabla E(\mathbf{k}(t'))\mathrm{d}t')a^c_{\mathbf{k}}(t). \end{aligned} \tag{4}$$

Here, $\Omega_R(\mathbf{k}(t)) = \frac{d_x(\mathbf{k}(t))E_x(t)}{\hbar}$ is Rabi frequency, in which $d_x(\mathbf{k}(t) = \langle\Psi^v_{\mathbf{k}_0}|ex|\Psi^c_{\mathbf{k}}\rangle$ is the wavenumber-dependent transition dipole matrix element and has the following form of

$$d_x(\mathbf{k}) = \frac{ea}{2\sqrt{3}}\frac{1+\cos(\frac{ak_y}{2})[\cos(\frac{\sqrt{3}ak_x}{2} - 2\cos(\frac{ak_y}{2})]}{1+4\cos(\frac{ak_y}{2})[\cos(\frac{\sqrt{3}ak_x}{2} + \cos(\frac{ak_y}{2})]}. \tag{5}$$

$\nabla E(\mathbf{k}) = E_c(\mathbf{k}) - E_v(\mathbf{k})$ is the characteristic energy difference between conduction band and valence band.

In the undoped graphene before laser excitation, all states in the valence band are completely occupied and those in the conduction band are empty. One can numerically solve the above differential equations (equation (4)) to obtain the dynamic occupation of electrons in conduction band as $\rho^c_{\mathbf{k}}(t) = |a^c_{\mathbf{k}}(t)|^2$. The investigated residual current density is defined as $j_x = -\frac{2e}{(2\pi)^2}\int_{\mathrm{BZ}}\rho^c_{\mathbf{k}}(t_\infty)v_x\mathrm{d}\mathbf{k}$ [6, 7], with v_x being the velocity along the k_x direction in momentum space, given by the slope of the conduction band $v_x = \frac{\partial E_c(k_x)}{\partial k_x}$. The magnitude of this residual current is determined by the integration of the residual occupation of electrons in

conduction band over the first Brillouin zone (BZ), indicating that the more asymmetric the occupation is, the larger its magnitude is.

2.3. Dirac approximation

However the above proposed numerical simulation is much complicated and time-consumption, it is not a good choice for clarifying the complex phenomena disclosed as follows, an approximate treatment to the form factor $f(\mathbf{k})$ is quite necessary. Now the Dirac approximation [25, 26] is adopted and $f(\mathbf{k})$ can be approximated as the first order term of the Taylor series expansion at the valley point $\mathbf{K}(0, \frac{4\pi}{3a})$ with $f(\mathbf{K}) = 0$. The field-free Hamilton is then rewritten as

$$H_0 = \hbar v_F \begin{bmatrix} 0 & k_x - \mathrm{i}k_y \\ k_x + \mathrm{i}k_y & 0 \end{bmatrix} = \hbar v_F \begin{bmatrix} k_y & -k_x \\ -k_x & -k_y \end{bmatrix}. \tag{6}$$

$v_F = \frac{\varepsilon_h \sqrt{3}\, a}{2\hbar}$ ($\approx 1e^6$ m s^{-1}) is Fermi velocity around **K** point. Because here the external field is x-directional polarized, only k_x is influenced by external field, and thus the time-dependent Hamilton changes as

$$H(t) = \hbar v_F \begin{bmatrix} k_y & -k_x(t) \\ -k_x(t) & -k_y \end{bmatrix}, \tag{7}$$

similar with those for a series of two-level atomic systems with different eigen-energy differences, whose bandgap is $\Delta = 2\hbar v_F k_y$ and the time-dependent Rabi frequency is $\Omega_R(t) = \hbar v_F k_x(t) \approx e v_F A_x(t)$, with $_{Ax}$ being the vector potential of the external field.

3. Results and discussion

As for the numerical simulation, the external chirped laser pulse [27] is presently defined as

$$E_x = E_0 \exp\left(-\frac{t^2}{\tau_p^2}\right) \cos\left(\omega_0 t + \frac{\alpha t^2}{2} + \varphi_0\right), \tag{8}$$

without loss of generality, linearly polarized along the x direction. Here E_0, ω_0, and τ_p indicate the field strength, central frequency and pulse duration, respectively. φ_0 is the CEP. α is the chirp rate and it makes the carrier-wave frequency being time-dependent. If $\alpha > 0$, the laser pulse is up-chirped, otherwise down-chirped. Thus, tuning the chirp rate, the light-field waveform will be broadened or compressed in the sub-cycle time scale, compared with that for a transform-limited pulse. It can be expected that this chirp-dependent laser waveform would and should show a significant influence on the current generated in graphene, however whether this influence is or not similar to that from CEP [7]. In the following investigation, the chirp rate is tuned within the range from -0.07 to 0.07 fs^{-2} but setting φ_0 (CEP)as zero in order to make difference from those in [7].

In addition, we choose that the central photon energy $\hbar\omega_0$ is 1.5 eV (~800 nm wavelength) and the pulse duration, τ_p, is 5 fs, much shorter than the characteristic electron scattering time of several tens femtoseconds for graphene [3]. Such few-cycle pulses have already occurred routinely in laboratory or commercially [28, 29] via the well-developed self-phase modulation technique via rare-gas-filled hollow fiber or capillary combined with dispersion compensation via chirped mirrors quite early for a relatively high intensity enough for strong laser physics. Beyond photon frequency and pulse duration, another essential parameter is laser field strength E_0, which is adopted as 2.4 V nm^{-1} in the following, larger enough to ensure the electron dynamics in graphene well within the so-called light-field-driven regime [7], where $\Omega_R > \omega_0$ is a prerequisite and simultaneously the perturbative theory loses efficacy. Thus a defined critical field strength E_{0c} when $\Omega_R = \omega_0$, can be estimated as $E_{0c} = \frac{\hbar\omega_0^2}{e v_F} \approx 1.8$ V nm^{-1}. This value is consistent with that numerically demonstrated in figure 2(a), at which the residual current reverses its direction.

3.1. Non-monotonic increase of residual current

Now we start to investigate the influence of initial laser chirp rate on the residual current in graphene. In figure 2, we plot the residual current as a function of field strength under different chirp rates. From this figure (especially the inset of (a)), one can easily find that when the field strength increases,the current first increases, and then decreases until to around 1.8 V nm^{-1} at which the current reverses its direction, and further increase in the opposite direction. As a whole, the current versus field strength exhibits a non-monotonic increase pattern. Such a non-monotonic increase pattern in graphene is quite different from those under weak-field excitation [6], where a monotonic increase pattern is induced due to the one-photon and two-photon absorption interference, indicated by $|j_x| \propto E_0^3$ in figure 2(b). In addition, one can see that when the field strength exceeds 1.8 V nm^{-1}, the variance of residual current with field strength is more sensitive to chirp rate. Since the chirp-dependent current

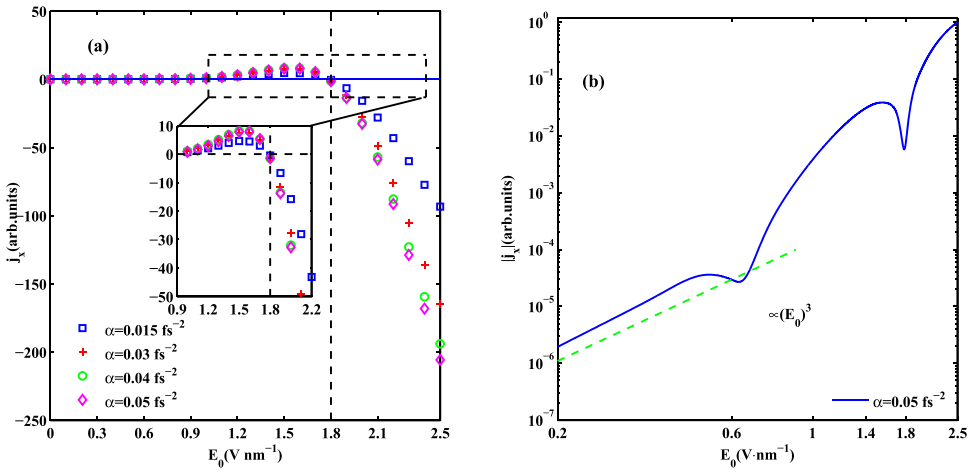

Figure 2. (a) Residual current as a function of the peak electric field strength E_0 for different chirp rates in the range of 0–2.5 V nm^{-1}. The direction of residual current evidently reverses at $E_0 \approx 1.8$ V nm^{-1}, clear shown in the drawing of partial enlargement. Such the field strength is not dependent on the chirp rate. (b) Log–log plot of residual current $|j_x|$ (solid line) versus E_0, when field strength is weak, $|j_x| \propto E_0^3$ (dashed line). When the field strength is strong, the cubic dependence is broken.

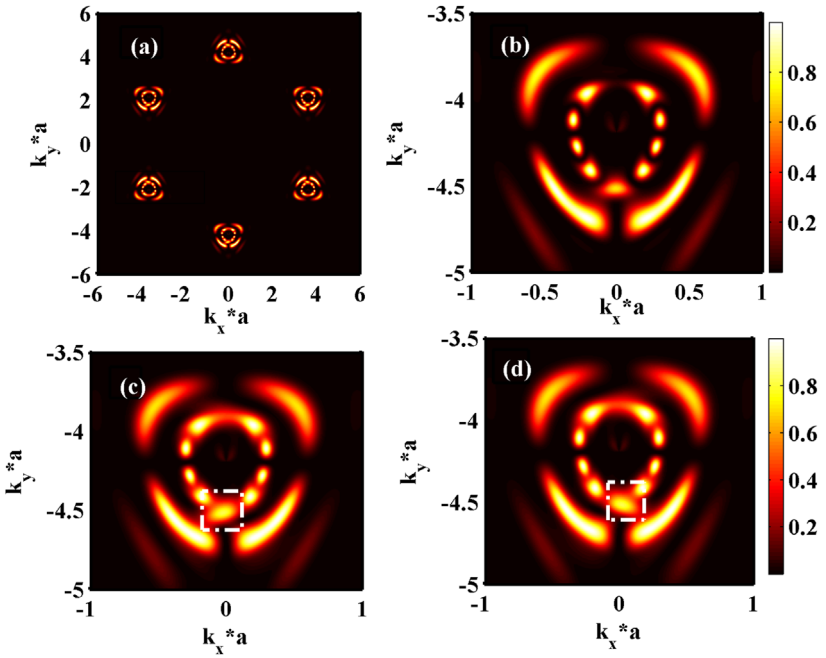

Figure 3. Simulated distribution of residual conduction population ρ_{CB} for different initial chirp rates. Population distribution in (a) full Brillouin zone for $\alpha = 0.00$ and in single valley K′ point for (b) $\alpha = 0.00$, (c) $\alpha = -0.05$ fs^{-2}, and (d) $\alpha = 0.05$ fs^{-2}.

in graphene is our main focus of investigation, this is another reason why we set the field strength E_0 as 2.4 V nm^{-1}.

To understand why the residual current is sensitive to chirp rates under enough high field strength, one can refer to investigate the residual occupation of electrons in conduction band, because the magnitude of current is determined by the integration of the residual occupation of electrons over the first BZ and the more asymmetric the occupation is, the larger the magnitude of current is. Therefore, we investigated the residual population of electrons under different chirp rates, as shown in figure 3.

If chirp-free ($\alpha = 0$), that is the incident laser pulse is transform-limited, the population distribution is mirror symmetric along the laser polarization direction. Thus, the obtained residual current after integration over the first BZ is zero. Moreover, from inner to outside, clear ring-shaped but intensity-modulated distributions are presented in figures 3(a) and (b) which corresponding to one-photon absorption, two-photon absorption, and so on. However, when an initial chirp rate is introduced, such as $\alpha = \pm 0.05$ fs^{-2}, the population distribution becomes asymmetric along the k_x axis, manifested especially in the dashed square areas

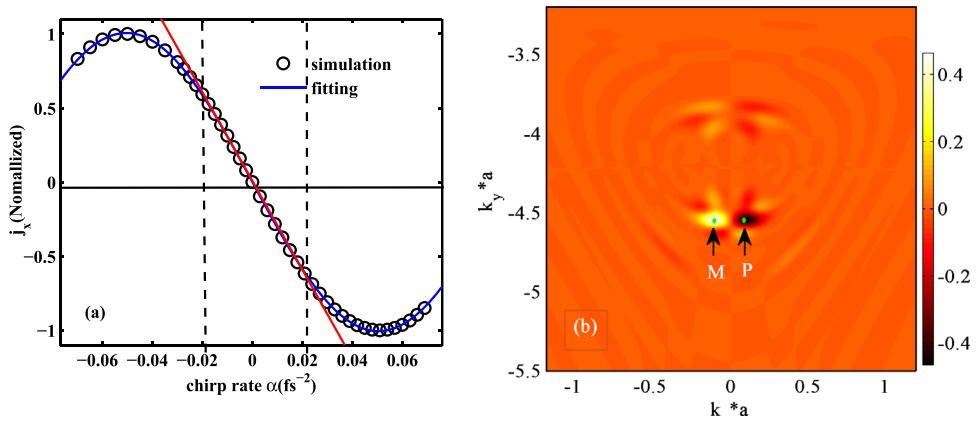

Figure 4. (a) Simulated residual current versus chirp rate, which is perfectly fitted by a sinusoidal function of $\sin(\kappa\alpha)$ (κ is around 31.13 for the simulation parameters here). (b) Residual population difference of $\rho_{CB}(0.05\ \mathrm{fs}^{-2})-\rho_{CB}(-0.05\ \mathrm{fs}^{-2})$.

in figures 3(c) and (d), where the residual population distributions present clear slope, and the slope values for positive chirp ($\alpha = 0.05\ \mathrm{fs}^{-2}$) and negative chirp ($\alpha = -0.05\ \mathrm{fs}^{-2}$) are with the opposite sign but the same magnitude (figure 4(a)).

With a small step change of chirp rate in the range of from -0.07 to $0.07\ \mathrm{fs}^{-2}$, one can get a more clear relationship between the residual current and chirp rate, as shown in figure 4(a). It is obviously that the current is very sensitive to chirp rate. More interesting, the whole chirp-dependence can be well fitted by a perfect sinusoidal function, $\sin(\kappa\alpha)$ with κ is a suitable fitting factor. If chirp rate is small enough ($|\alpha| \leqslant 0.02\ \mathrm{fs}^{-2}$), this chirp-dependence is simplified further as $\kappa\alpha$, indicating that the residual current is directly proportional to chirp rate, referring to the eye-guiding line in figure 4(a).

3.2. Chirp dependent Landau–Zener–Stückelberg interference

There naturally occur two questions, one is why the residual current is chirp-dependent, and the other is why this chirp-dependence follows a sinusoidal function pattern. In the following, the underlying mechanism for them is disclosed in three steps.

Step 1: as in the above demonstration, the residual conduction band population distribution is mirror asymmetric along the k_x axis when an initial chirp rate is introduced (figure 3), and this asymmetry is chirp-rate-dependent. This point will be more clear if one making the chirp-dependent conduction band population difference, for example, between $\alpha = 0.05\ \mathrm{fs}^{-2}$ and $\alpha = -0.05\ \mathrm{fs}^{-2}$ [figure 4(b)]. In this condition, the population in $-k_x$ direction is larger than that in $+k_x$ direction, especially in regions around points M and P, leading to a negative current along x direction.

Step 2: considering these two points P and M as examples, because they play the dominant contributions to the final asymmetric population distributions. Beyond this, the LZS interference is investigated to find the clues for the chirp-rate-dependence of residual current. In case of graphene, the transition probability can be estimated as $\exp(-\pi\Delta^2/4\hbar^2\omega\Omega_R)$ [7, 23]. The electron dynamics driven by the external field follow the LZ formula, especially under condition of $\Delta \approx \sqrt{\omega\Omega_R}$, in which the electrons tend to pass the avoided crossings (i.e. bandgap minima), one part jumps non-adiabatically into the conduction band, while the rest still stays adiabatically in the valence band. As for a linearly polarized excitation, electrons can always repeatedly pass the avoided crossings within one optical period, leading the different excitation quantum pathways. These quantum pathways can interfere and thus the final distribution of population in the conduction would be sensitively dependent on the phase relationship among these pathways. To obtain the insight of LZS interference in light-field-driven regime, we need know the information of temporal evolution of the conduction band population and phase accumulation at P and M point. The case of LSZ interference is determined by two-phase terms One is the transition phase $\Delta\varphi_T$ (known as stokes phase) for a single LZ process between valence and conduction band, and the other is the propagation phase described as $\Delta\varphi_P = 1/\hbar\int_{t_1}^{t_2} E_c(\mathbf{k}(t')) - E_v(\mathbf{k}(t'))\mathrm{d}t'$. Here t_1 and t_2 refer to the moments of two LZ transition events, and E_c and E_v represent the momentum-dependent energies of conduction and valence band states. Figure 5 shows the conduction band population and the propagation phase as a function of time for two different initial point M and P. For the trajectory starting from point M, the two mainly transition events at approximately $t_2 = -0.12$ fs and $t_2 = 1.51$ fs in figure 5(a). The propagation phase accumulation from t_1 to t_2 is π (figure 5(b)), and then plus the additional transition phase π from the LZ transition, the total phase accumulation would be 2π. Therefore, a constructive interference is induced. A larger population in conduction band occurs (figure 5(c), M point). In contrast, the total phase accumulation is 3π

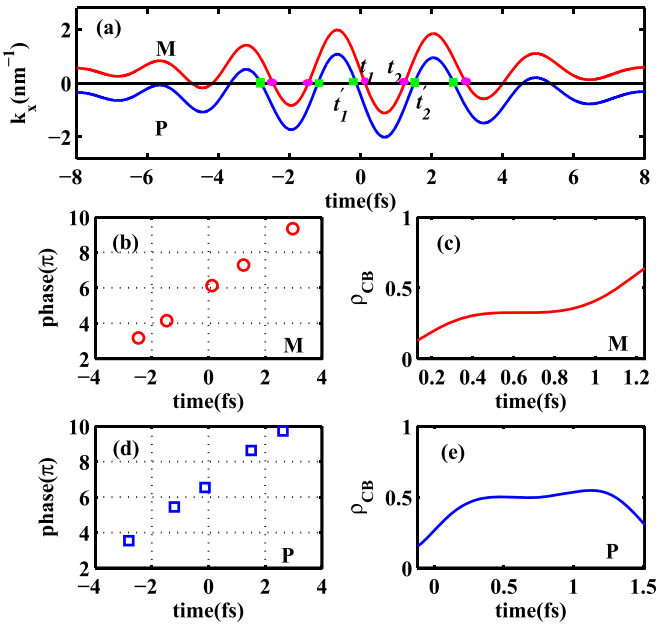

Figure 5. (a) Two representative electron trajectories starting from points M and P in figure 4 with circle and square points representing that moments at which electrons reach band minima and transit between valence band and conduction band. (b), (d) The propagation phase accumulated from initiation to the above respective transition moment. Conduction band population ρ_{CB} (c) for point M resulting from constructive interference mainly determined by phase difference between t_1 and t_2, and (e) ρ_{CB} for point P from destructive interference mainly by phase difference between t_1' and t_2'. Here chirp rate $\alpha = 0.05$ fs^{-2}.

from the start point P (figure 5(d)), resulting in a destructive interference and thus a smaller population in conduction band (figure 5(e), P point). This kind of quantum phase difference for start points M and P finally lead to the occurrence of asymmetric population distribution in the strong field regime.

Step 3: now let us answer why the relation between residual current versus chirp rate follows a sinusoidal function. As demonstrated above, the chirp-dependent residual asymmetric conduction-band population distribution originate in the pathways interference. In the following, we will explicitly write the chirp-dependent phase analytically. We define the magnitude D of residual population in conduction band in single **k** state (i.e. M or P point in figure 4(b)) in condition of two pathways $D = |\mathbf{A}_1| + |\mathbf{A}_2| + 2|\mathbf{A}_1||\mathbf{A}_2|\cos(\theta)$, with $\mathbf{A}_1$ and $\mathbf{A}_2$ indicating pathways probability amplitude between $(-\infty, t_1)$ and $(-\infty, t_2)$ and $\theta = \Delta\varphi_T + \Delta\varphi_P$. D depends on their relative phase θ. The transition phase $\Delta\varphi_T$ is π, determined by the sign of electric field, which presents the avoided crossings [6], does not have difference with or without chirp rate. Therefore, we only focus on the propagation phase. If the laser field is x polarized and the Dirac approximation is assumed

$$\triangle\varphi_P = 2\frac{\epsilon_h}{\hbar}\int_{t_1}^{t_2}|f[\mathbf{k}(t')]|\mathrm{d}t' \approx 2\epsilon_h \mathbf{v}_F\int_{t_1}^{t_2}\sqrt{k_x^2(t') + k_y^2}\,\mathrm{d}t', \tag{9}$$

only k_x is time dependent and k_y is assumed as 0, the $\triangle\varphi_P$ can be rewritten as

$$\triangle\varphi_P \approx 2\epsilon_h \mathbf{v}_F\int_{t_1}^{t_2}|k_x(t')|\mathrm{d}t' = 2\epsilon_h \mathbf{v}_F\int_{t_1}^{t_2}|k_x - A_x(t')|\mathrm{d}t', \tag{10}$$

the integration term presents variation of electron momentum between transitions at time t_1 and t_2, and only has the same sign (positive or negative). Thus, the absolute sign can be ignored, and assume initial wave vector $k_x = 0$. Since the vector potential $_{Ax}(t)$ takes the form $A_x(t) = \frac{E_0}{\omega_0}g(t)\sin(\omega_0 t + \frac{\alpha}{2}t^2)$, the above formula for propagation phase can be expanded as

$$\begin{aligned}\triangle\varphi_P = 2\epsilon_h \mathbf{v}_F\int_{t_1}^{t_2}\frac{eE_0}{\hbar\omega_0}g(t')[\sin(\omega_0 t')\cos(\frac{\alpha}{2}t'^2)\\ + \cos(\omega_0 t')\sin(\frac{\alpha}{2}t'^2)]\mathrm{d}t',\end{aligned} \tag{11}$$

where $g(t)$ is envelop of the laser pulse, which does not depends on chirp rate. If the chirp rate is small, one can further rewrite it as

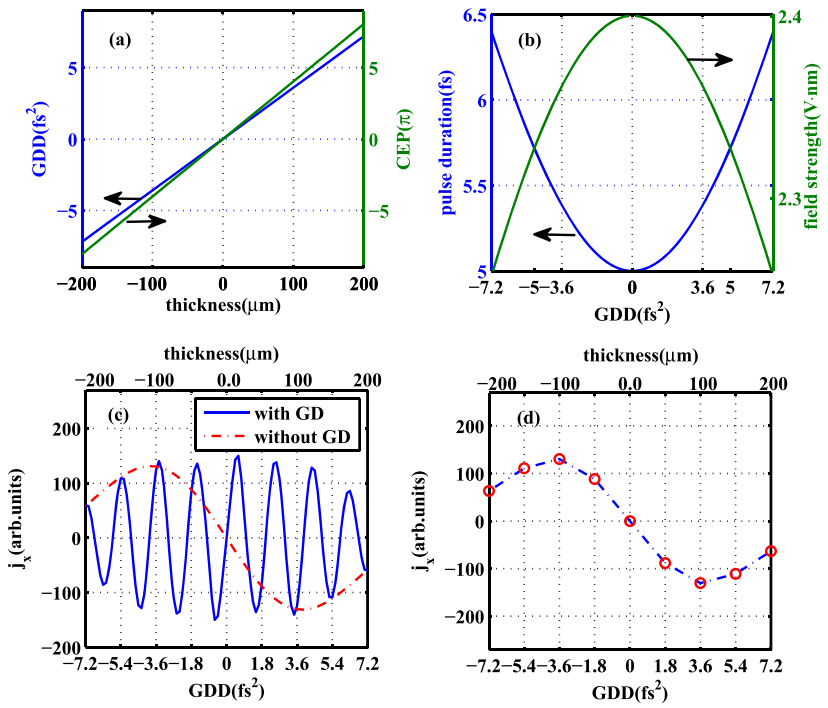

Figure 6. (a) GDD and CEP as a function of thickness of fused silicon d; (b) pulse duration and field strength as a function of GDD; (c) simulated chirp-dependent residual current in graphene with (solid line) and without GD (dashed–dotted line); (d) simulated chirp-dependent residual current but with only phases integer number of 2π selected from (c), where the current only depends on the chirp rate.

$$\begin{aligned}\triangle\varphi_P &= 2\epsilon_h \mathbf{v}_F \frac{eE_0}{\hbar\omega_0}\int_{t_1}^{t_2} g(t')\sin(\omega_0 t')\mathrm{d}t' + \epsilon_h \mathbf{v}_F \alpha \frac{eE_0}{\hbar\omega_0}\int_{t_1}^{t_2} g(t')t'^2\cos(\omega_0 t')\mathrm{d}t' \\ &= c_1 + \alpha c_2 \propto \alpha, \end{aligned} \tag{12}$$

with c_1 and c_2 are some constants. Thus, D is qualitatively proportional to $\cos(\alpha)$. Based on the definition of residual current j_x, the magnitude of j_x is determined by the asymmetry of the distribution of residual population, i.e. mainly determined the difference between critical k points(e.g. P and M point). Therefore, the residual current follows sinusoidal function shape.

Above all, via these three steps, the origin for the sinusoidal of chirp-rate-dependence of residual current is clarified. The questions of why the residual current is chirp-dependent and why this chirp-dependence follows a sinusoidal function pattern have been completely answered.

3.3. More practical introduction of chirp rate

In all the above investigation, the carrier-envelope phase is fixed as zero but just the chirp rate is tuned. However, in reality, this is not true. For example, when the chirp rate is introduced via dispersive media and characterized by group delay dispersion (GDD), the CEP is also simultaneously introduced [30], as shown in figure 6(a). Thus electron dynamics in graphene would and should be influenced by both CEP and chirp rate, and the investigation of the isolated role of chirp or CEP is made complicated. Therefore it is necessary to investigate them simultaneously. Taking fused silicon as an example of dispersive media, and how the chirp rate and CEP as well as the residual current change with the thickness of fused silicon [30], is demonstrated in details.

As a start, the laser pulse after propagating through fused silicon can be expressed in frequency-domain as, $E_{\mathrm{Chirp}}(\omega) = E_{\mathrm{TL}}(\omega, \varphi_0)\exp(-\mathrm{i}\phi(\omega))$. Here, E_{TL} describes the transform-limited pulse and φ_0 is just the initial CEP (here is set as zero). $\phi(\omega)$ is the phase induced by dispersion in fused silicon and can be expanded as a Taylor series, $\phi\Big(\omega) = \phi_0 + (\omega - \omega_0)\phi_1 + \frac{1}{2}(\omega - \omega_0\Big)^2\phi_2$, up to the second-order approximation. ϕ_0 is a constant phase shift and can be set as zero without loss of generality. ϕ_1 is group delay (GD) which is related to the change of CEP when propagating through media. In contrast, ϕ_2 is group delay dispersion (GDD), which introduces the linear chirp. The propagation distance or the thickness of fused silicon can influence the values of GD and GDD, and thus one can change the thickness to tune the chirp rate of the incident laser pulse.

After the definition of the chirped pulse in frequency-domain, we can get the expression of the electric field in time-domain via the fast Fourier transformation (FFT) algorithm. Then we add some new calculations, as shown in figure 6, where how the chirp rate and CEP as well as the residual current change are investigated in detail when tuning the thickness of fused silicon in the range of $d = [-200, 200]$ μm. One point needs to point

out is that in order to check the similarity or difference with our previous calculation, the parameters for field strength, pulse duration, central wavelength, and so on (before propagating through fused silicon) are kept same.

As shown in figure 6(a), the CEP and GDD versus the thickness of fused silicon d follows a linear proportional way, and when the thickness of fused silicon d change by 100 μm, the CEP will changes by 4π and GDD by 3.6 fs^2 approximatively. From the above new definition of chirped laser, one easily obtain the variance of field strength and pulse duration with GDD (figure 6(b)). When the thickness d increases, the field strength E_0 decreases and pulse duration increases, as expected from energy conservation. The residual current j_x of main focus is recalculated shown in figure 6(c). Without GD (or CEP is fixed as zero as before), the residual current shows a sine-functional dependence on GDD (dashed–dotted line), which is qualitatively consistent with that in figure 3(a) and if with GD (solid line), sine-functional dependence pattern is modulated by CEP, which is disclosed experimentally [7].

Further, if one want to isolate the influences of CEP and chirp rate on the current in graphene. For example, to investigate the only chirp- dependent current without the influence of CEP, one feasible way is to suitably control the thickness of fused silicon to ensure the phase equal to $2n\pi$ (n is an integer, $n = 0, 1, \cdots$), due to the fact that the residual current would be zero if for a transform-limited (without chirp rate) laser pulse. So that the influence of CEP can be eliminated if we only focus on the influence from chirp rate. The corresponding simulation to the only-chirp dependent current is shown in figure 6(d). The residual current versus GDD also exhibit a sine-functional pattern.

From this new calculation, one can see that the original sine-functional dependence of residual current on chirp rate is reproduced under a more practical situations and the conclusion obtained above is kept invariant.

4. Conclusion

In conclusion, we have numerically demonstrated that the electron dynamics in graphene can be controlled by adjusting the chirp rate of a few-cycle driving laser. In the light-field-driven regime, the chirp-dependent LZS interference causes the occurrence of an asymmetric residual current. Moreover, the directionality of such a chirp dependent residual current changes in a sine-functional way. Note that the feasibility of experiment is also discussed. Even to consider a more realistic situation, the main conclusions keep invariant. This theoretical demonstration of ultrafast current control on the sub-cycle timescale will provide a meaningful guidance in the future experimental confirmation and development of solid-state petahertz optoelectronic metrology.

Acknowledgments

The work is supported by National Natural Science Foundation of China (Grants Nos.11674342 and 61775087)

ORCID iDs

Erheng Wu https://orcid.org/0000-0002-4888-5034
Chaojin Zhang https://orcid.org/0000-0003-2774-9380
Zhanshan Wang https://orcid.org/0000-0002-2161-6934
Chengpu Liu https://orcid.org/0000-0003-1814-7177

References

[1] Zener C 1934 *Proc. R. Soc.* A **145** 523–9
[2] Keldysh L *et al* 1965 *Sov. Phys. JETP* **20** 1307–14
[3] Kruchinin S Y, Krausz F and Yakovlev V S 2018 *Rev. Mod. Phys.* **90** 021002
[4] Wu M, Ghimire S, Reis D A, Schafer K J and Gaarde M B 2015 *Phys. Rev.* A **91** 043839
[5] Mücke O, Tritschler T, Wegener M, Morgner U and Kärtner F 2001 *Phys. Rev. Lett.* **87** 057401
[6] Wismer M S, Kruchinin S Y, Ciappina M, Stockman M I and Yakovlev V S 2016 *Phys. Rev. Lett.* **116** 197401
[7] Higuchi T, Heide C, Ullmann K, Weber H B and Hommelhoff P 2017 *Nature* **550** 224
[8] Ghimire S, DiChiara A D, Sistrunk E, Agostini P, DiMauro L F and Reis D A 2011 *Nat. Phys.* **7** 138
[9] Schiffrin A *et al* 2013 *Nature* **493** 70
[10] Schultze M *et al* 2013 *Nature* **493** 75
[11] Krausz F and Stockman M I 2014 *Nat. Photon.* **8** 205
[12] Schultze M *et al* 2014 *Science* **346** 1348–52
[13] Schubert O *et al* 2014 *Nat. Photon.* **8** 119
[14] Luu T T, Garg M, Kruchinin S Y, Moulet A, Hassan M T and Goulielmakis E 2015 *Nature* **521** 498
[15] Vampa G, Hammond T, Thiré N, Schmidt B, Légaré F, McDonald C, Brabec T and Corkum P 2015 *Nature* **522** 462

[16] Hohenleutner M, Langer F, Schubert O, Knorr M, Huttner U, Koch S, Kira M and Huber R 2015 *Nature* **523** 572
[17] Vampa G, Hammond T, Thiré N, Schmidt B, Légaré F, McDonald C, Brabec T, Klug D and Corkum P 2015 *Phys. Rev. Lett.* **115** 193603
[18] Sun D, Divin C, Rioux J, Sipe J E, Berger C, De Heer W A, First P N and Norris T B 2010 *Nano Lett.* **10** 1293–6
[19] Heide C, Higuchi T, Weber H B and Hommelhoff P 2018 *Phys. Rev. Lett.* **121** 207401
[20] Zhang C and Liu C 2016 *Phys. Lett.* A **380** 3233–7
[21] Dimitrovski D, Madsen L B and Pedersen T G 2017 *Phys. Rev.* B **95** 035405
[22] Bartels R, Backus S, Zeek E, Misoguti L, Vdovin G, Christov I, Murnane M and Kapteyn H 2000 *Nature* **406** 164
[23] Shevchenko S, Ashhab S and Nori F 2010 *Phys. Rep.* **492** 1–30
[24] Houston W 1940 *Phys. Rev.* **57** 184
[25] McCann E 2011 Electronic properties of monolayer and bilayer graphene *Graphene Nanoelectronics* (Berlin: Springer) pp 237–75
[26] Yang H, Feng X, Wang Q, Huang H, Chen W, Wee A T and Ji W 2011 *Nano Lett.* **11** 2622–7
[27] Lara-Astiaso M, Silva R, Gubaydullin A, Riviere P, Meier C and Martin F 2016 *Phys. Rev. Lett.* **117** 093003
[28] Sartania S, Cheng Z, Lenzner M, Tempea G, Spielmann C, Krausz F and Ferencz K 1997 *Opt. Lett.* **22** 1562–4
[29] Yamane K, Zhang Z, Oka K, Morita R, Yamashita M and Suguro A 2003 *Opt. Lett.* **28** 2258–60
[30] Abdelrahman Z, Khokhlova M, Walke D, Witting T, Zair A, Strelkov V, Marangos J and Tisch J 2018 *Opt. Express* **26** 15745–58